Research Article | Vol. 9, No. 8 | 1 Aug 2018 | BIOMEDICAL OPTICS EXPRESS 3821
Biomedical Optics EXPRESS

Volumetric macro- and micro-scale assessment of crystalline lens opacities in cataract patients using long-depth-range swept source optical coherence tomography

IRENEUSZ GRULKOWSKI,[1] SILVESTRE MANZANERA,[2] LUKASZ CWIKLINSKI,[1] JUAN MOMPEÁN,[2] ALBERTO DE CASTRO,[2] JOSE MARIA MARIN,[3] AND PABLO ARTAL[2,*]

[1]*Institute of Physics, Faculty of Physics, Astronomy and Informatics, Nicolaus Copernicus University, ul. Grudziądzka 5, 87-100 Toruń, Poland*
[2]*Laboratorio de Óptica, Instituto Universitario de Investigación en Óptica y Nanofísica, Universidad de Murcia, Campus de Espinardo, E-30100 Murcia, Spain*
[3]*Servicio de Oftalmología, Hospital Universitario "Virgen de la Arrixaca", E-30100 Murcia, Spain*
**pablo@um.es*

Abstract: We demonstrate an optimized optical platform for the three-dimensional (3-D) visualization of crystalline lens opacities in vivo in the eyes of patients with different types and grades of cataracts. We developed a prototype long-depth-range swept source optical coherence tomography (SS-OCT) instrument operating at the speed of 50 kA-scans/second and at the central wavelength of 1 μm to perform high-resolution imaging of the whole anterior segment of the eye. Volumetric data sets of cataractous eyes were acquired and processed to obtain contrast-enhanced high-resolution images of lenticular structures and opacifications. The results showed lens micro- and macro-scale features related to possible cataract development such as cortical spokes, water clefts and enhanced scattering in the lens nucleus. The results demonstrate also the ability of this SS-OCT imaging to locate and characterize opacities quantitatively. The instrument might be a useful tool in the high-resolution preoperative evaluation of crystalline lens opacities in cataract patients.

OCIS codes: (110.4500) Optical coherence tomography; (120.3890) Medical optics instrumentation; (120.4820) Optical systems; (170.4470) Ophthalmology.

References and links

1. S. Bassnett, Y. Shi, and G. F. J. M. Vrensen, "Biological glass: structural determinants of eye lens transparency," Philos. Trans. R. Soc. Lond. B Biol. Sci. **366**(1568), 1250–1264 (2011).
2. R. Michael and A. J. Bron, "The ageing lens and cataract: a model of normal and pathological ageing," Philos. Trans. R. Soc. Lond. B Biol. Sci. **366**(1568), 1278–1292 (2011).
3. P. Artal, "Optics of the eye and its impact in vision: a tutorial," Adv. Opt. Photonics **6**(3), 340–367 (2014).
4. P. Artal, "Image Formation in the Living Human Eye," Annu Rev Vis Sci **1**(1), 1–17 (2015).
5. L. T. Chylack, Jr., J. K. Wolfe, D. M. Singer, M. C. Leske, M. A. Bullimore, I. L. Bailey, J. Friend, D. McCarthy, and S. Y. Wu, "The lens opacities classification system III," Arch. Ophthalmol. **111**(6), 831–836 (1993).
6. B. Masters, "Three-dimensional microscopic tomographic imagings of the cataract in a human lens in vivo," Opt. Express **3**(9), 332–338 (1998).
7. J. L. Alió, P. Schimchak, H. P. Negri, and R. Montés-Micó, "Crystalline lens optical dysfunction through aging," Ophthalmology **112**(11), 2022–2029 (2005).
8. B. J. Kirkwood, P. L. Hendicott, S. A. Read, and K. Pesudovs, "Repeatability and validity of lens densitometry measured with Scheimpflug imaging," J. Cataract Refract. Surg. **35**(7), 1210–1215 (2009).
9. D. S. Grewal, G. S. Brar, and S. P. S. Grewal, "Correlation of nuclear cataract lens density using Scheimpflug images with lens opacities classification system III and visual function," Ophthalmology **116**(8), 1436–1443 (2009).
10. P. Rosales and S. Marcos, "Pentacam Scheimpflug quantitative imaging of the crystalline lens and intraocular lens," J. Refract. Surg. **25**(5), 421–428 (2009).

#332330 https://doi.org/10.1364/BOE.9.003821
Journal © 2018 Received 22 May 2018; revised 17 Jul 2018; accepted 17 Jul 2018; published 24 Jul 2018

Biomedical Optics EXPRESS

11. X. Weiner, M. Baumeister, T. Kohnen, and J. Bühren, "Repeatability of lens densitometry using Scheimpflug imaging," J. Cataract Refract. Surg. **40**(5), 756–763 (2014).
12. C. V. Harding, L. T. Chylack, Jr., S. R. Susan, W. K. Lo, and W. F. Bobrowski, "Elemental and ultrastructural analysis of specific human lens opacities," Invest. Ophthalmol. Vis. Sci. **23**(1), 1–13 (1982).
13. A. Antunes, M. G. Hönnicke, A. M. V. Safatle, C. Cusatis, P. S. Moraes Barros, and S. L. Morelhão, "Diffraction enhanced X-ray imaging of mammals crystalline lens," Nucl. Instrum. Methods Phys. Res. Sect. B **238**(1), 28–31 (2005).
14. Y. E. Lee and C.-K. Joo, "Assessment of lens center using optical coherence tomography, magnetic resonance imaging, and photographs of the anterior segment of the eye," Invest. Ophthalmol. Vis. Sci. **56**(9), 5512–5518 (2015).
15. M. De La Hoz Polo, A. Torramilans Lluís, O. Pozuelo Segura, A. Anguera Bosque, C. Esmerado Appiani, and J. M. Caminal Mitjana, "Ocular ultrasonography focused on the posterior eye segment: what radiologists should know," Insights Imaging **7**(3), 351–364 (2016).
16. T. J. T. P. Van Den Berg, L. J. Van Rijn, R. Michael, C. Heine, T. Coeckelbergh, C. Nischler, H. Wilhelm, G. Grabner, M. Emesz, R. I. Barraquer, J. E. Coppens, and L. Franssen, "Straylight effects with aging and lens extraction," Am. J. Ophthalmol. **144**(3), 358–363 (2007).
17. T. J. T. P. van den Berg, L. Franssen, B. Kruijt, and J. E. Coppens, "History of ocular straylight measurement: A review," Z. Med. Phys. **23**(1), 6–20 (2013).
18. P. Artal, A. Benito, G. M. Pérez, E. Alcón, A. De Casas, J. Pujol, and J. M. Marín, "An objective scatter index based on double-pass retinal images of a point source to classify cataracts," PLoS One **6**(2), e16823 (2011).
19. O. Sahin, A. Pennos, H. Ginis, L. Hervella, E. A. Villegas, B. Cañizares, J. M. Marin, I. Pallikaris, and P. Artal, "Optical Measurement of Straylight in Eyes With Cataract," J. Refract. Surg. **32**(12), 846–850 (2016).
20. F. Cabot, A. Saad, C. McAlinden, N. M. Haddad, A. Grise-Dulac, and D. Gatinel, "Objective assessment of crystalline lens opacity level by measuring ocular light scattering with a double-pass system," Am. J. Ophthalmol. **155**(4), 629–635 (2013).
21. F. Galliot, S. R. Patel, and B. Cochener, "Objective scatter index: working toward a new quantification of cataract?" J. Refract. Surg. **32**(2), 96–102 (2016).
22. J. M. Bueno, D. De Brouwere, H. Ginis, I. Sgouros, and P. Artal, "Purkinje imaging system to measure anterior segment scattering in the human eye," Opt. Lett. **32**(23), 3447–3449 (2007).
23. R. R. Ansari, M. B. Datiles, J. F. King, and D. Leftwood, "Measuring lens opacity: combining quasi-elastic light scattering with Scheimpflug imaging system," Proc. SPIE **3246**, 35–42 (1998).
24. R. R. Ansari, K. I. Suh, S. Dunker, N. Kitaya, and J. Sebag, "Quantitative molecular characterization of bovine vitreous and lens with non-invasive dynamic light scattering," Exp. Eye Res. **73**(6), 859–866 (2001).
25. M. B. Datiles 3rd, R. R. Ansari, and G. F. Reed, "A clinical study of the human lens with a dynamic light scattering device," Exp. Eye Res. **74**(1), 93–102 (2002).
26. D. Huang, E. A. Swanson, C. P. Lin, J. S. Schuman, W. G. Stinson, W. Chang, M. R. Hee, T. Flotte, K. Gregory, C. A. Puliafito, and J. G. Fujimoto, "Optical coherence tomography," Science **254**(5035), 1178–1181 (1991).
27. W. Drexler, M. Liu, A. Kumar, T. Kamali, A. Unterhuber, and R. A. Leitgeb, "Optical coherence tomography today: speed, contrast, and multimodality," J. Biomed. Opt. **19**(7), 071412 (2014).
28. I. Grulkowski, "Anterior segment OCT," in *Handbook of Visual Optics, Volume Two: Instrumentation and Vision*, P. Artal, ed. (CRC Press - Taylor & Francis Group, 2016).
29. I. Grulkowski, M. Gora, M. Szkulmowski, I. Gorczynska, D. Szlag, S. Marcos, A. Kowalczyk, and M. Wojtkowski, "Anterior segment imaging with Spectral OCT system using a high-speed CMOS camera," Opt. Express **17**(6), 4842–4858 (2009).
30. A. de Castro, S. Ortiz, E. Gambra, D. Siedlecki, and S. Marcos, "Three-dimensional reconstruction of the crystalline lens gradient index distribution from OCT imaging," Opt. Express **18**(21), 21905–21917 (2010).
31. I. Grulkowski, J. J. Liu, B. Potsaid, V. Jayaraman, C. D. Lu, J. Jiang, A. E. Cable, J. S. Duker, and J. G. Fujimoto, "Retinal, anterior segment and full eye imaging using ultrahigh speed swept source OCT with vertical-cavity surface emitting lasers," Biomed. Opt. Express **3**(11), 2733–2751 (2012).
32. P. Pérez-Merino, M. Velasco-Ocana, E. Martinez-Enriquez, and S. Marcos, "OCT-based crystalline lens topography in accommodating eyes," Biomed. Opt. Express **6**(12), 5039–5054 (2015).
33. M. Sun, J. Birkenfeld, A. de Castro, S. Ortiz, and S. Marcos, "OCT 3-D surface topography of isolated human crystalline lenses," Biomed. Opt. Express **5**(10), 3547–3561 (2014).
34. C. D. Dicarlo, W. P. Roach, D. A. Gagliano, S. A. Boppart, D. X. Hammer, A. B. Cox, and J. G. Fujimoto, "Comparison of optical coherence tomography imaging of cataracts with histopathology," J. Biomed. Opt. **4**(4), 450–458 (1999).
35. A. L. Wong, C. K.-S. Leung, R. N. Weinreb, A. K. C. Cheng, C. Y. L. Cheung, P. T.-H. Lam, C. P. Pang, and D. S. C. Lam, "Quantitative assessment of lens opacities with anterior segment optical coherence tomography," Br. J. Ophthalmol. **93**(1), 61–65 (2009).
36. D. V. Palanker, M. S. Blumenkranz, D. Andersen, M. Wiltberger, G. Marcellino, P. Gooding, D. Angeley, G. Schuele, B. Woodley, M. Simoneau, N. J. Friedman, B. Seibel, J. Batlle, R. Feliz, J. Talamo, and W. Culbertson, "Femtosecond laser-assisted cataract surgery with integrated optical coherence tomography," Sci. Transl. Med. **2**(58), 58ra85 (2010).

Biomedical Optics EXPRESS

37. Y. N. Kim, J. H. Park, and H. Tchah, "Quantitative Analysis of Lens Nuclear Density Using Optical Coherence Tomography (OCT) with a Liquid Optics Interface: Correlation between OCT Images and LOCS III Grading," J. Ophthalmol. **2016**(3025413), 3025413 (2016).
38. J. R. Kuszak, R. K. Zoltoski, and C. E. Tiedemann, "Development of lens sutures," Int. J. Dev. Biol. **48**(8-9), 889–902 (2004).
39. N. A. Frost, J. M. Sparrow, and L. Moore, "Associations of human crystalline lens retrodots and waterclefts with visual impairment: An observational study," Invest. Ophthalmol. Vis. Sci. **43**(7), 2105–2109 (2002).
40. G. F. J. M. Vrensen, "Early cortical lens opacities: a short overview," Acta Ophthalmol. **87**(6), 602–610 (2009).
41. R. Michael, R. I. Barraquer, B. Willekens, J. van Marle, and G. F. J. M. Vrensen, "Morphology of age-related cuneiform cortical cataracts: The case for mechanical stress," Vision Res. **48**(4), 626–634 (2008).
42. A. de Castro, A. Benito, S. Manzanera, J. Mompeán, B. Cañizares, D. Martínez, J. M. Marín, I. Grulkowski, and P. Artal, "Three-dimensional cataract crystalline lens imaging with swept-source optical coherence tomography," Investig. Ophthalmol. Vis. Sci. **59**(2), 897–903 (2018).
43. I. Grulkowski, S. Manzanera, L. Cwiklinski, F. Sobczuk, K. Karnowski, and P. Artal, "Swept source optical coherence tomography and tunable lens technology for comprehensive imaging and biometry of the whole eye," Optica **5**(1), 52 (2018).

1. Introduction

Transparency of the human crystalline lens is provided by a specific organization of the lenticular cells, which limits both light scattering and absorption [1,2]. Cataract is developed by the formation of opacifications of the crystalline lens, which becomes less transparent. Light propagating in the cataractous lens becomes diffused, which also degrades the contrast in the retinal image and affects visual quality [3,4]. Age-related cataracts are leading causes of blindness nowadays affecting more than half the population of 75 + yo. The standard treatment of cataracts is based on the surgical replacement of the crystalline lens with an artificial intraocular lens.

The methods for detection and evaluation of cataract *in vivo* can be classified into two groups: imaging-based techniques and straylight measurement approaches. The first group utilizes images of the crystalline lens acquired with different technologies. Current clinical evaluation of lenticular opacities is mostly based on eye examination using slit-lamp microscopy. The subjective analysis of slit-lamp images of the lens is a basis for the cataract classification systems, e.g. Lens Opacification Classification System (LOCS III) [5]. Scheimpflug imaging enables visualization of the crystalline lens, and quantitative assessment of opacification can be performed with lens densitometry [6–11]. The other lens imaging modalities include x-ray imaging, magnetic resonance imaging or B-mode ultrasound although they demonstrate several issues that limit their clinical utility [12–15].

The second group comprises the methods that measure degradation of the retinal image quality due to higher intraocular scattering. Straylight (forward scatter) component is determined objectively by implementation of a single parameter such as log(s) or the objective scatter index, which represents general behavior of the light beam propagating in the ocular media and does not provide any spatially resolved information [16–18]. The concept of straylight measurement is used in the commercial systems like C-Quant (Oculus GmbH, Germany) or Optical Quality Analysis System – High Definition Analyzer (Visiometrics SL, Spain) that have been introduced to clinical practice to assess intraocular scattering [17,19–21]. The analysis of Purkinje images enables also determination of the corneal and lenticular contribution to intraocular scattering without any impact of the retina (as in the double-pass systems) [22]. The intensity of halo around the fourth Purkinje image (P_{IV}) increases with the amount of scattering. Finally, dynamic light scattering due to Brownian motion is applied to analyze changes in the lens on the molecular level since it can determine the size distribution of crystallins, which correlates with early formation of cataract [23–25].

Detection of back-scattered photons is at the foundation of optical coherence tomography (OCT) – an infrared interferometric modality that nowadays constitutes a clinical standard in early detection of retinal pathologies [26,27]. The development of OCT technologies enable cross-sectional (2-D) and three-dimensional (3-D) visualization of the ocular structures in the

Biomedical Optics EXPRESS

anterior segment and the retina [28]. OCT imaging of the anterior segment of the eye (including the crystalline lens) has been demonstrated in animal models and in humans using spectral-domain OCT (SD-OCT) and swept-source OCT (SS-OCT) [29–33]. In addition, attempts for qualitative and quantitative assessment of OCT images of cataract eyes have been presented but the studies were usually confined to the analysis of single cross-sectional images [34–37]. However, opacifications can appear as multifocal micrometer spots in the crystalline lens, and some early forms of cataract are located in the lens periphery that develop towards the visual axis. Therefore, 2-D imaging of cataract eyes does not explore full potential of current technology, and it may lead to incorrect diagnosis.

In this paper, we demonstrate comprehensive visualization of crystalline lens opacities *in vivo* in patients with different types of cataracts. We utilize a prototype long-depth-range SS-OCT instrument developed to perform 3-D (volumetric) imaging of the whole anterior segment of the eye. We also present visualization strategies to enhance image contrast related to lens opacifications, and to identify features of lenticular macro- and micro-morphology in different types of cataracts.

2. Methods

2.1 Prototype SS-OCT instrument for anterior segment imaging

We developed a long-range SS-OCT system (Fig. 1) which used a customized wavelength-swept light source operating at the central wavelength of 1050 nm (bandwidth 110 nm) and at the sweep rate of 50 kHz (duty cycle 60%; Axsun Technologies Inc., USA). The reduction of the sweeping rate (from standard 100 kHz to 50 kHz) enabled achieving a longer coherence length of the source. An asymmetric fiber-optic Michelson interferometric configuration (with the splitting ratio 80:20 between the arms) was used in the instrument to assure the power incident on the cornea (1.9 mW) did not exceed ANSI standards. The detection and acquisition subsystem consisted of a balanced photodetector (PDB-480-C, Thorlabs Inc., USA) and a digitizer of 0.8 GS/s bandwidth (National Instruments, USA). A built-in FPGA module enabled real-time preview (Fig. 1(a)). Additionally, the initial alignment of the subject eye was provided by the iris camera implemented in the interface of the instrument. The depth range of the system was 22.2 mm in air. The obtained sensitivity was 103 dB, and the signal roll-off was −6 dB at 11 mm. The measured axial and transverse resolutions in air were 8 μm and 43 μm, respectively.

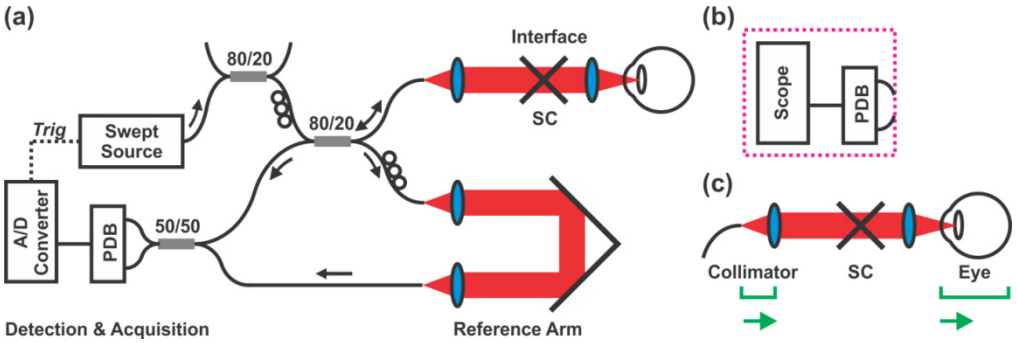

Fig. 1. Experimental set-up. (a) Prototype SS-OCT system for whole anterior segment imaging. PDB – balanced photodetector, SC – galvanometric scanners, 80/20 – fiber coupler. (b) Detection configuration for the measurement of the coherence function of the swept light source. (c) Details of the experiment aiming at optimization of the objective lens in the SS-OCT system interface (sample arm).

2.2 Optimization of the set-up

The optimization stage of the SS-OCT system was required to address the challenges of full anterior segment imaging. The entire procedure included minimizing the signal drop with

Biomedical Optics EXPRESS

depth and the choice of the optimum illumination optics. The real signal roll-off $S_{SS\text{-}OCT}(z)$ in SS-OCT is characterized by the factors like: instantaneous coherence function $C(z)$ of the light source, bandwidths of the photodetector $S_{PDB}(z)$ and acquisition card $S_{ADC}(z)$ as well as by the light intensity distribution $S_{illum}(z)$ provided by the optics in the sample arm:

$$S_{SS-OCT}(z) = C(z) \cdot S_{illum}(z) \cdot S_{PDB}(z) \cdot S_{ADC}(z). \quad (1)$$

The first test of the set-up was the measurement of the coherence length of the light source. We used a fiber-optic interferometer with ultrahigh-bandwidth electronics (Fig. 1b). Therefore, the interferometric fringes were detected with a dual-balance photodetector (PDB480C-AC, Thorlabs Inc., USA) and recorded by a scope (WaveMaster 804Zi-A, LeCroy GmbH, Germany) for different optical path differences. The normalized amplitude of the fringe $C(z)$ indicates that −6 dB signal drop is observed at the depth (2·OPD) of 14 mm (Fig. 2a). Later on, the reference mirror was moved in 1 mm steps, and the fringes were acquired using the actual imaging system with the detection and acquisition set-up described in Section 2.1 (Fig. 1a). The point-spread functions demonstrate that significant differences between the coherence function and the signal roll-off in our instrument is present for the depths higher than 18 mm (Fig. 2a). It means that we do not have significant inherent signal drop at the distances corresponding to anterior segment depth, and the system design provides practically a coherence-function-limited signal drop with depth.

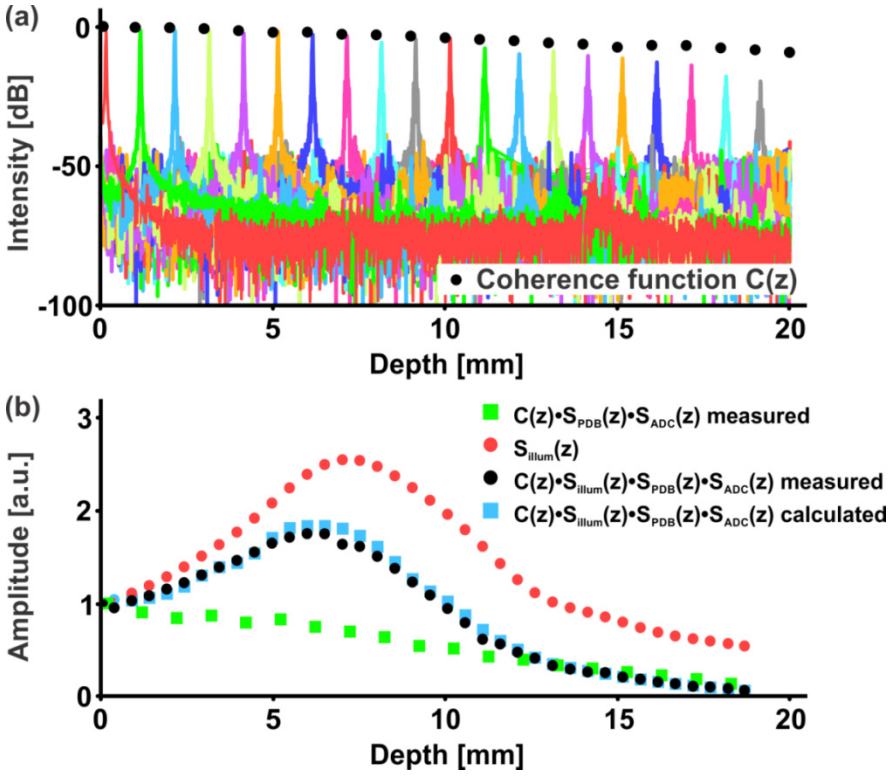

Fig. 2. Performance of the SS-OCT instrument for anterior segment imaging. (a) Coherence function (dotted) and signal roll-off with depth. (b) Impact of different factors on signal drop for optimum system configuration. The legend corresponds to the symbols used in Eq. (1).

The optimization procedure enabled also the choice of an objective lens to assure uniform illumination of the imaged volume and sufficient photon collection efficiency. We imaged the left eye of the same 34 yo subject for different positions of the focus vs. the eye. In the experiment, current eye position was compensated by a translation of the collimator in the

Biomedical Optics EXPRESS

sample arm whereas the reference arm length was kept constant (Fig. 1(c)). Consequently, it was possible to examine only the impact of the depth of focus on the OCT image quality. The results demonstrate that the system interface with the lens of longer focal distance (f = 150 mm) is less sensitive to eye positioning vs. focus (Fig. 3). Accordingly, the objective lens with focal length f = 150 mm was used in the following experiments. Moreover, the focus should be located ca. 7 mm away from the zero path difference plane to obtain the most optimum quality of the whole anterior segment image.

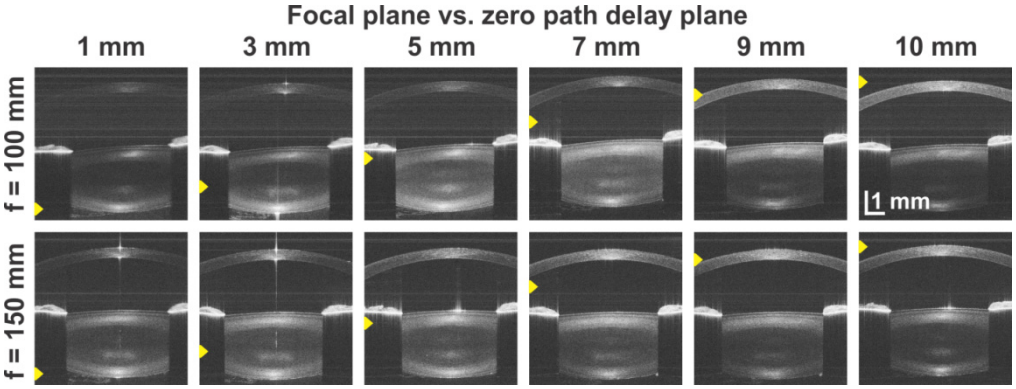

Fig. 3. Optimization of the objective lens. Images of the entire anterior segment of the eye for different positions of the eye vs. focal plane. The signal position vs. zero delay line was kept constant to be independent on the signal drop with depth. The image quality is more degraded when shorter focal length objective is used in the sample arm.

Implementing the above-mentioned observations into the SS-OCT system, we determined real signal roll-off by measuring both interferometric fringes and the light intensity collected from the sample arm for different positions of the mirror in the sample arm. The data were normalized to the case at zero path difference. The plots in Fig. 2(b) demonstrate real signal roll-off $S_{SS\text{-}OCT}(z)$ in the instrument, total light intensity collected from the sample arm and previously measured detection signal roll-off. The fringe amplitude is given by the following relation:

$$I(k,z) \propto \sqrt{I_s(k) I_r(k)} \cos(2kz) \qquad (2)$$

where I_s and I_r are intensities in the sample and reference arm, respectively, k is the wavenumber and z is the optical path difference. Therefore, we calculated the square root of axial intensity profile and multiplied with detection signal roll-off. The calculated roll-off coincided very well with the measured signal drop (blue and black dots in Fig. 2(b)).

2.3 Scanning procedures

We imaged 50 eyes of 30 participants (mean age: 60 ± 18 yo; age range: 26-91 yo): subjects and cataract suspects without / with lens opacifications (12; mean age: 50 ± 21 yo; age range: 26-81 yo) or cataract patients before surgery (18; mean age: 67 ± 12 yo; age range: 36-91 yo). No eye dilation was induced in subjects and cataract suspects during the experiments, and the measurements were performed under dimmed room lighting to avoid possible pupillary constriction. On the other hand, the cataract patients were scanned preoperatively after pupil dilation with 1% Tropicamide and a standard clinical examination. The procedures were approved by the institutional review board at the University of Murcia. The research adhered to the tenets of the Declaration of Helsinki. Each participant was informed about the nature of the study, and a written informed consent was obtained before imaging.

Biomedical Optics EXPRESS

We used two types of scan protocols: high-definition (HD) cross-sectional images and 3-D volumetric data sets of the anterior segment covering 8 × 8 mm^2 or 16 × 16 mm^2 area (1900 × 50 A-scans for HD protocol or 300 × 300 A-scans for 3-D protocol, respectively).

2.4 Data processing

Initially, we reviewed the B-scans in the data set to make sure that no corneal opacities were present. Then, the lateral motion correction of B-scans in volumetric data sets was performed by manual shifting of the affected B-scans to obtain a circular shape of the pupil in the *en-face* image. On the other hand, residual axial motion artifacts were corrected automatically based on extracted slow scan cross-section. Next, the crystalline lens signal only from the pupil area was taken into account since the crystalline lens signal is shadowed by the hyper-reflective iris (Fig. 4(a)).

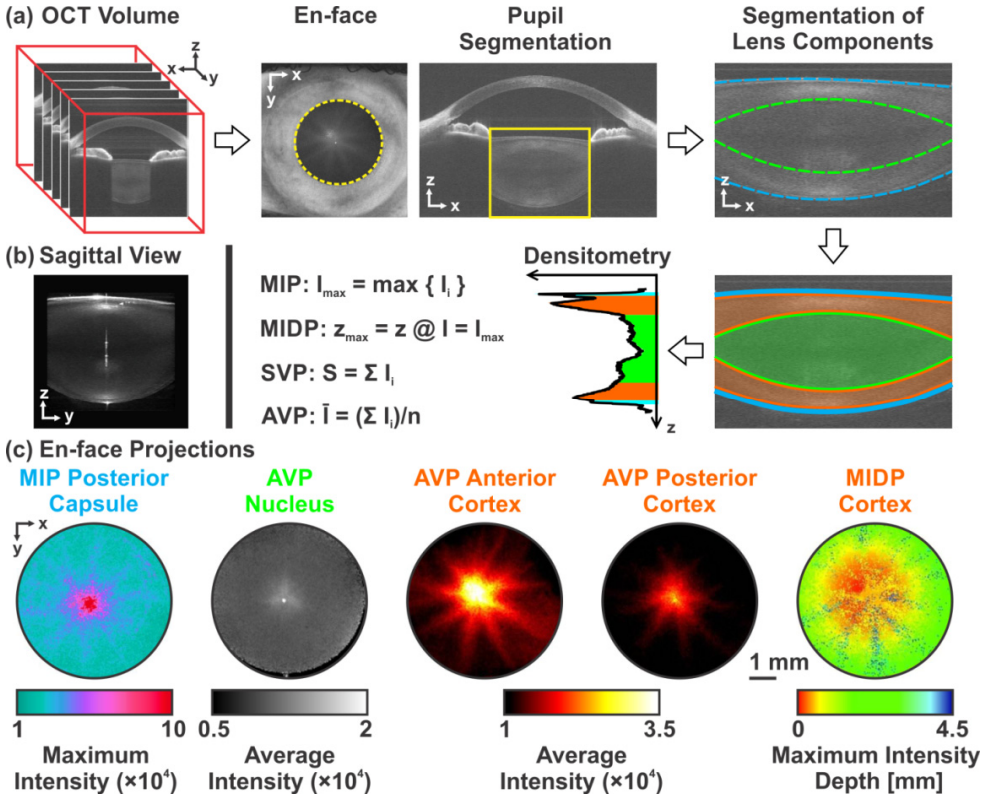

Fig. 4. Post-processing of volumetric SS-OCT data of the 26-yo healthy young subject. (a) Signal from the lens of the motion-corrected volumetric data is segmented. Anterior and posterior capsule, anterior and posterior cortex and the nucleus are segmented to enable determination of different parameters in those components (Visualization 1). (b) Sagittal (side) projection (MIP) of the crystalline lens. (c) Examples of *en-face* projections of the lens capsule, nucleus and the cortex. Images were not corrected for light refraction.

Then, anterior and posterior interfaces of the crystalline lens were segmented using edge detection. The nucleus of the crystalline lens was segmented by semi-automated fitting of two elliptic paraboloid surfaces. This was achieved in practice by a two-step process. First, the manual fitting two parabolas (anterior and posterior nucleus) in both perpendicular central cross-sections (horizontal and vertical) of the pupil area was done. Later on, the segmentation in other B-scans was obtained automatically by a simple axial shift of parabolas from horizontal central B-scan, and the shift was supposed to reveal the segmented parabola in vertical section. Thus, we were able to divide the crystalline lens into its anatomical

Biomedical Optics EXPRESS

components including: anterior and posterior capsule (both defined as the layer around anterior / posterior lens interface of the thickness of 260 μm, respectively), anterior and posterior cortex and the nucleus (Fig. 4(a) and Visualization 1). Such a virtual lens decomposition permitted calculation of parameters like maximum signal (intensity), the depth at which maximum intensity is found, voxel intensity sum and average voxel intensity for each part of the lens. In particular, central pupil area could be averaged to generate a densitogram (densitometric profile) or maximum OCT signal along sagittal (x) direction could be extracted to obtain side projection (y-z) (Fig. 4(b)). In addition, the following *en-face* lenticular projections (x-y) could be generated: maximum intensity projection (MIP), maximum intensity depth projection (MIDP; measured from the anterior capsule), sum voxel projection (SVP) or average intensity projection (AVP) (Fig. 4(c)).

3. Results

3.1 Healthy young subject

The eyes of 7 subjects (mean age: 35 ± 6 yo; age range: 26-44 yo) with no lenticular opacification were imaged. As an example, the left eye of a 26 yo volunteer was scanned with long-range SS-OCT instrument to visualize the crystalline lens of a healthy young subject. Different visualization strategies of volumetric data included the rendered 3-D view, *en-face* view and averaged central cross-section of the anterior segment spanning the entire transverse anterior chamber width (Fig. 4(a)). The anatomical details of the crystalline lens such as the capsule, cortex and nucleus can be easily distinguished and identified. The OCT signal in those components do not reveal any inhomogeneity, and the lens nucleus is less reflective than the cortex (Fig. 4(a)). Visualization 1 includes a rendering of a volumetric data set, in which the crystalline lens has been segmented and colored, and the fly-through clearly demonstrates OCT signal homogeneity of the lens and the segmentation of the capsule, the cortex and the nucleus. Side view of the crystalline lens, being equivalent to slit lamp image, illustrates the clarity of the lens (Fig. 4(b)). On the other hand, characteristic star-shaped pattern in both cortex *en-face* projections is observed, that can be associated with the crystalline lens sutures and fibers (Fig. 4(c)) [38].

3.2 Cataract suspects

We also imaged 5 cataract suspects (mean age: 71 ± 11 yo; age range: 55-81 yo) who have not been diagnosed with cataract at the time of OCT scanning. The images in Fig. 5 illustrate age-related changes in the crystalline lens. OCT cross-sections show different morphology features of the aging lens. The lenticular opacifications appear as hyper-reflective region directing from the lens periphery toward the center (Fig. 5(a)). In another case presented here, the signal in the anterior cortex becomes less homogeneous across the lateral direction, which indicates that the regular organization of the collagen fibrils is disturbed (Fig. 5(b)). Moreover, small volumes demonstrating hypo-reflectivity can be associated with vacuoles. Sagittal view of maximum intensity is characterized by a higher signal in the lens nucleus that is prerequisite for nuclear opacifications (Fig. 5(c)).

Biomedical Optics EXPRESS

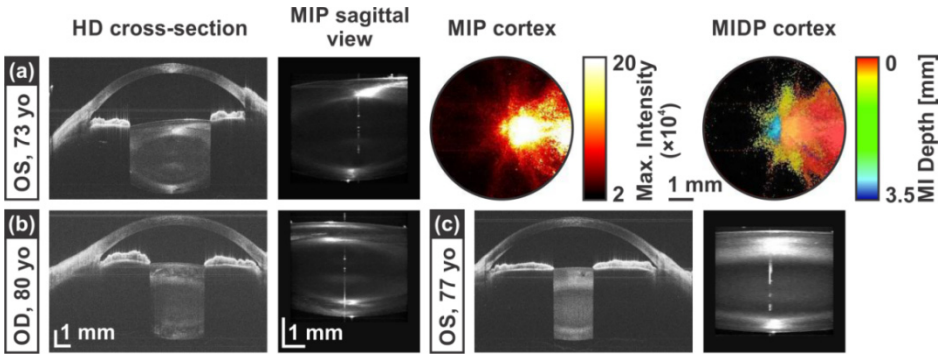

Fig. 5. SS-OCT imaging of the eyes of cataract suspects. (a) Left eye of 73-yo subject. (b) Right eye of 80-yo subject. (c) Left eye of 77-yo subject. High-definition cross-sectional images. MIP sagittal views and *en-face* MIP map and MIDP of the cortex overlaid with maximum intensity map. Images were not corrected for light refraction.

3.3 Cataractous eyes

Cataracts are primarily categorized into three types depending on which anatomical zone of the crystalline lens is obscured by the opacification. We imaged 18 patients with diagnosed age-related cataracts. Cataract grading was completed by an experienced ophthalmologist in accordance to the LOCS III system. In this section, we demonstrate the performance of SS-OCT system to visualize different types of cataract and we present the features of cataractous lens morphology.

The lens opacities confined to the cortex form cortical cataract. Some microstructural changes typical for cortical cataract were already demonstrated (cf. Fig. 5). The data sets in Fig. 6(a)-(b) show opacification of the crystalline lens typical for cortical cataract. Cross-sectional images indicate hyper-intensive layer-like deposits that may cause shadowing effect in OCT images (Fig. 6(a)). Those cortical spokes visible in the *en-face* MIDP views are characterized by highly scattering radially oriented wedge-shaped regions located either in the anterior or posterior part of the cortex (Fig. 6(a)-(b) and Visualization 2). The spokes (cuneiform opacities) are initially formed in the equatorial (peripheral) zone of the lens, and during cataract progression they extend towards the pupillary area limiting the vision significantly. The opacifications in the anterior cortex can also be accompanied by hypo-intensive regions, called water clefts, which are optically transparent (Fig. 6(b)-6(c)). In addition to that, enhanced scattering is observed in the cortex at the posterior pole of the lens (Fig. 6(c)).

In the nuclear cataract, the central part of the crystalline lens becomes cloudy and yellow over time. The opaque lens nucleus should exhibit more scattering, thus being easily detectable in OCT. The imaging of an eye with advanced nuclear cataract is illustrated in Fig. 6(d). The cross-sectional image as well as the sagittal MIP show significantly higher signal in the lens nucleus of cataractous eyes. This is especially distinctive if one compares sagittal projections of the lens of the nuclear cataract patient (Fig. 6(d)) with corresponding sagittal projections of the eyes of cataract suspects (Fig. 5).

The last group contains the opacities subjacent to the lens capsule at the posterior pole. Posterior subcapsular cataract patient was a 36 yo female. The opacifications manifest here as increased scattering observed just beneath the lens capsule. The nucleus of the lens is clear with some microstructural changes demonstrated as separated dot opacities (Fig. 7(a)). The subcapsular cataract can also be visualized in the cross-sectional images as hyperintensive anterior and / or posterior interface of the lens (Visualization 3). This type of opacification is shown clearly in maximum intensity projection maps associated with the anterior or posterior capsule (Fig. 7(b)).

Biomedical Optics EXPRESS

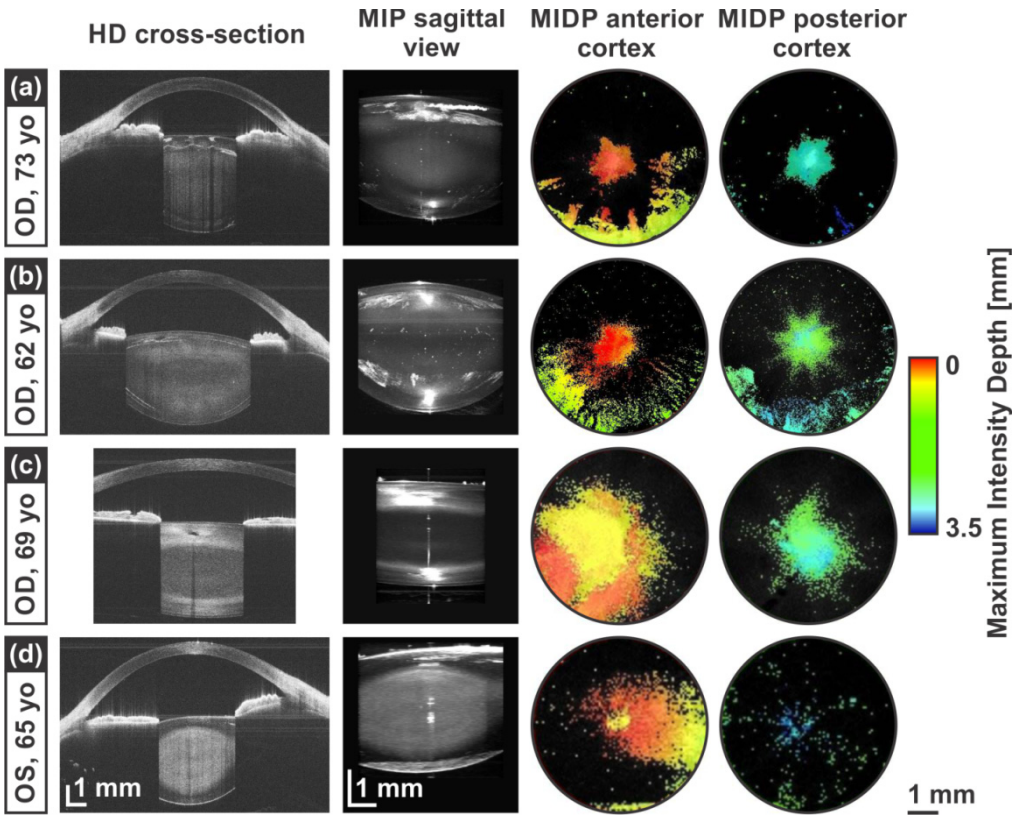

Fig. 6. SS-OCT imaging of cortical and nuclear cataract in the lens. (a) Cortical and nuclear (mixed) cataract in right eye of 73-yo patient. (b) Cortical cataract in the right eye of 62-yo patient (Visualization 2). (c) Cortical cataract in the right eye of 69-yo patient. (d) Nuclear cataract in left eye of 65-yo patient. The columns represent: HD cross-sectional image, MIP sagittal view, MIDP overlaid with maximum intensity map for anterior and posterior cortex (brightness indicates maximum intensity). Images were not corrected for light refraction.

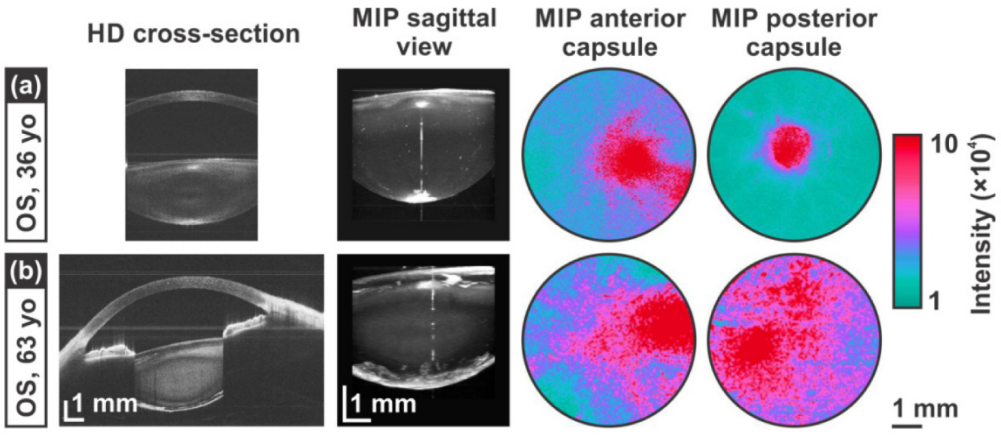

Fig. 7. SS-OCT imaging of subcapsular cataract. (a) Left eye of 36-yo patient. (b) Left eye of 63-yo patient (Visualization 3). The columns represent: HD cross-sectional image, MIP sagittal view, MIP map of the anterior and posterior capsule. Images were not corrected for light refraction.

Additionally, inspection of recorded cataract features in Figs. 5-7 implies that cataracts can occur in combinations. The analyzed 3-D data sets revealed the eyes with mixed

Biomedical Optics EXPRESS

cataracts. Severe cortex opacities are associated with the higher nuclear opalescence (Figs. 6(a), 6(d), 7(b)) or with unusually high reflectivity of lens capsule (Figs. 6(d), 7(b)).

Finally, we demonstrate an overview of the projection maps of representative eyes for different grades of cataract according to LOCS III scheme (Fig. 8). We have selected different SS-OCT data visualization modes that facilitate quantitative assessment of previously mentioned cataract types. The cortical cataract was represented by maximum intensity projection taken from anterior and posterior cortex. This was supplemented with the maximum intensity depth map. The cortical MIPs reveal that the degree of cortical opacification is associated with the affected pupillary zone (Fig. 8(a)). Cortical opacifications at higher grades take up a dominant part of the pupil area, which impacts the visual performance. Moreover, the nuclear opalescence was mapped using average voxel projections, which become brighter for more opaque nuclear cataract. More advanced nuclear cataract is characterized by a more opacified nucleus that scatters more light, and this is clearly indicated in the cross-sectional images and the projection map. Finally, maximum intensity projection of the posterior capsule was chosen to visualize opacities in posterior subcapsular cataract. In this case, the opacified area gets larger for higher grades in LOCS III scale (Fig. 8(a)).

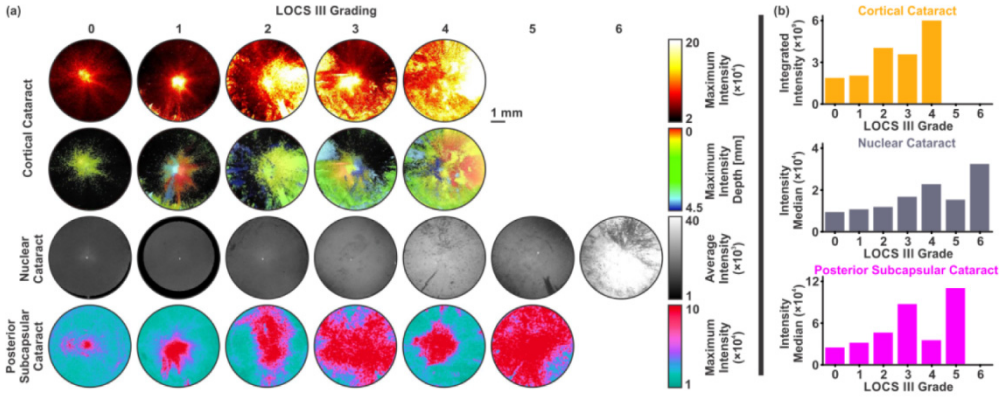

Fig. 8. Quantitative analysis of SS-OCT volumetric data of crystalline lenses (a) Representative SS-OCT *en-face* projection maps of crystalline lenses of patients with different cataract types and grades. Rows from the top represent: MIP and MIDP maps of the cortex, AVP map of the nucleus and MIP map of the posterior capsule. (b) Dependence of the integrated maximum intensity of the cortex, intensity median of the nucleus and the median of maximum intensity of the posterior capsule on the LOCS III grading. Images were not corrected for light refraction.

Quantification of the *en-face* projection enables determination of a single parameter that corresponds to the obtained LOCS III grade. Maximum intensities were integrated in cortical MIPs within the 5.5 mm-diameter circle. The same size of the zone was used to measure the nuclear opalescence by the median value in the obtained AVP. The median signal in the MIPs of the posterior capsule was also identified to represent the degree of opacification in that part of the crystalline lens. Those three selected parameters reveal the correspondence to the LOCS III grading although variability between the individuals is expected (Fig. 8(b)).

4. Discussion and conclusions

The SS-OCT technology developed in this study belongs to image-based techniques for *in vivo* evaluation of crystalline lens opacities at micro- and macro-scales. There are several advantages of the demonstrated modality in the cataract assessment.

Firstly, system optimization methodology enables long-depth-range three-dimensional imaging with micrometer resolution. The access to volumetric data allows for generating virtually any cross-section as well as *en-face* and / or side projection maps contrasted with

Biomedical Optics EXPRESS

different parameters. As a result, one can perform comprehensive investigation of the microstructural changes of the crystalline lens anatomy, which are related to the development of different types of cataracts.

Secondly, the developed post-processing algorithm aims at the effective visualization of crystalline lens opacities. Although it requires semi-automatic segmentation of the lens interfaces and the lens nucleus, it can provide both qualitative and quantitative information on lens opacification. Separate clinical study will implement the proposed approach to grade the cataracts objectively.

Thirdly, the swept source technology used in the OCT set-up enabled high detection sensitivity and reduced signal drop with depth. It causes the whole anterior segment to be effectively visualized unlike Scheimpflug imaging, in which it is hard to image posterior part of the crystalline lens. However, the wavelength of light used in the set-up had to be carefully chosen. The highest contrast of opacities can be obtained with shorter wavelengths using visible light, which would be equivalent to the scattering effects in the eye. The closest wavelength range from those traditionally applied in OCT would be around 800 nm. However, the availability of swept sources operating around 800 nm and characterizing sufficient instantaneous coherence length is very limited. Therefore, a tunable light source operating at 1050 nm was used in this study. Another advantage of using longer wavelengths is that generally higher power levels can be safely applied, which enhances the performance characteristics of the imaging system. Consequently, this allows for compensate for decreased light penetration in the case of severe and advanced cataract.

On the other hand, OCT imaging of the crystalline lens is limited by the iris, which determines numerical aperture of the eye, since the iris blocks the light to penetrate deeper. The shadows appear in the OCT images posterior to the iris, thus making visualization of the peripheral regions of the lens impossible. Therefore, the entire analysis is limited only to the pupil area, which can be made larger to some degree by application of mydriatics. This in turn prevents the studies of early processes of cataract formation that mainly take place in the periphery of the crystalline lens.

It has to be noted here that the optical platform used in this study operates on the detection of back-scattered light despite the fact that actually forward scatter reduces retinal image contrast, which is a direct indicator of intraocular opacification.

We visualized and identified different features characteristic for cataract formation such as cortical spokes, water clefts, vacuoles and enhanced scattering in the nucleus [39]. Those observations come from age-related modifications of microstructural morphology of the crystalline lens (at different organizational levels) [40,41]. The regular architecture of the lenticular cells (fibers) provides the transparency. However, in cortical cataract the disruption of the ultrastructure of the lens fibers due to their folding or breaking leads to the changes in scattering properties, which in turn impacts the SS-OCT images. In nuclear cataract, the local fluctuation of the crystallins and formation of aggregates seem to increase the scattering [2]. Finally, posterior subcapsular cataract is formed due to migration of metaplastic cells from the lens equator to the posterior pole, which causes production of defective fibers.

Preliminary results using this approach with less sophisticated analysis was applied to globally evaluate cataracts in another group of patients [42]. Apart from providing with the details of SS-OCT design optimized for opacity imaging, this report showed more advanced and more complex methodology of visualization of opacities located in different anatomical parts of the crystalline lens. Consequently, although no 3-D refraction correction algorithm was applied here, this approach allows for comprehensive analysis of lenticular opacifications attractive for clinicians. In addition, it is possible to extend the range of the instrument to obtain images of the retina and the vitreous areas. This was demonstrated by adapting a tunable lens into the optical setup [43].

In conclusion, we showed an optimized optical platform for versatile imaging of crystalline lens opacities. In particular, we demonstrated that 3-D long-depth-range SS-OCT

Biomedical Optics EXPRESS

technology enables volumetric visualization of *in vivo* macro- and microstructural changes in the crystalline lens related to opacification. Access to volumetric data allows for post-processing contrast enhancement due to the increased scattering inside the lens. Extraction of the quantitative information on the light back-scattering in lens components allows to consider SS-OCT as a lens opacity meter. The developed instrument has been optimized for crystalline lens imaging and can be considered as a useful tool in the high-resolution evaluation and management of the crystalline lens opacities in cataract patients. Quantification of opacities based on OCT images may help in diagnosing and grading cataract eyes.

Funding

European Research Council Advanced Grant (SEECAT, #ERC-2013-AdG-339228); Secretaría de Estado de Investigación, Desarrollo e Innovación (SEIDI; #FIS2016-76163-R); Fundación Séneca-Agencia de Ciencia y Tecnología de la Región de Murcia (#19897/GERM/15); European Regional Development Fund (#EU-FEDER); Polish Ministry of Science and Higher Education (Ministerstwo Nauki i Szkolnoctwa Wyższego; #IP2014 014073); Scholarship of the Polish Ministry for Science and Higher Education.

Disclosures

The authors declare that there are no conflicts of interest related to this article.